Interannual Variations of Monthly Precipitation and Associated Mechanisms over the Three River Source Region in China in Winter Months

Teng Wang[1,4], Bo Sun[1,2,3], Huijun Wang[1,2,3]

[1] Collaborative Innovation Center on Forecast and Evaluation of Meteorological Disasters/Key Laboratory of Meteorological Disasters, Ministry of Education/Joint International Research Laboratory of Climate and Environment Change, Nanjing University of Information Science and Technology, Nanjing 210044, China

[2] Nansen Zhu International Research Centre, Institute of Atmospheric Physics, Chinese Academy of Sciences, Beijing 100029, China

[3] Southern Marine Science and Engineering Guangdong Laboratory (Zhuhai), Zhuhai 519082, China

[4] Qamdo Meteorological Service, Qamdo 854000, China

[*]Corresponding author: Bo Sun, email: sunb@nuist.edu.cn

This article has been accepted for publication and undergone full peer review but has not been through the copyediting, typesetting, pagination and proofreading process which may lead to differences between this version and the Version of Record. Please cite this article as doi: 10.1002/joc.6954

Abstract This study investigates the interannual variability of winter precipitation over the Three River Source (TRS) region in China based on precipitation observations collected at stations in the TRS region and reanalysis datasets for the period of 1980–2015. The results suggest that the TRS winter precipitation has distinct interannual variability with discordant trends in different months, i.e., an increasing trend is found in November and February, a decreasing trend is found in other winter months, and interannual variations in precipitation are different in different months. The mechanisms for the interannual variation in monthly precipitation over the TRS region are significantly different in different winter months.

The interannual variability of TRS precipitation in November is modulated by an anomalous westerly water vapor transport (WVT) branch. This anomalous WVT branch is related to a North Atlantic-Europe-Tibetan Plateau (NA-E-TP) wave-train that originates in the North Atlantic due to the ocean-atmosphere interaction. In December, a circum-global teleconnection (CGT) wave-train can induce anomalous westerly WVT in the TRS region, resulting in increased precipitation there. This CGT wave-train is triggered by warm SST anomalies in the central-eastern tropical Pacific associated with the El Niño-Southern Oscillation (ENSO). The interannual variability of TRS precipitation in January and February is affected by southwesterly WVT anomalies over the TRS region, which are associated with a southeastward propagating wave-train over Eurasia caused by the North Atlantic Oscillation (NAO). In March, the interannual variability of TRS precipitation is modulated by the leading mode of the Eurasian circulation that resembles the Scandinavian (EU1) pattern, which can cause anomalous southwesterly WVT in the TRS region. In winter, the characteristics of sea surface temperature anomalies, weather systems, and atmospheric circulations associated with interannual variations of monthly precipitation in the TRS region are different for individual winter months.

Keywords Three River Source, Interannual variation, Winter precipitation, Atmospheric teleconnection, Water vapor transport

1. Introduction

The Three River Source (TRS) region is located in the south of Qinghai Province, China, which is also the heartland of the Tibetan Plateau (TP). The headwaters of the Yangtze River, Yellow River and Lantsang River connect in this region, where the geographic environment and climatic condition are unique. With a mean average elevation of 4000 m, combined with many rivers and lakes, topography is complex in the TRS region (Su *et al*., 2013; Tong *et al*., 2014). The TRS region provides water to natural ecosystems and more than one billion people in China and Southeast Asia. It plays an irreplaceable role in water conservation, runoff regulation, and ecological security (Liu *et al*., 2008; Jiang and Zhang, 2016). The vulnerability of the ecological environment in the TRS region is due to the special geographic location and unique environment of this region. As the TRS region is a national nature reserve, the underlying surface is almost unaffected by human activities. Climate change has become the most important factor affecting the ecological environment (Immerzeel *et al*., 2010; Hu *et al*., 2013). Previous studies have indicated that climate anomalies have affected the ecological balance and ecosystem in the TRS region (Zhang *et al*., 2011; Jiang *et al*., 2016). Many factors have affected local ecological security, such as changes in lake area (Liu *et al*., 2018), glacier shrinkage (Jiang and Zhang, 2015), permafrost degradation (Liu *et al*., 2018), and soil desertification (Liu *et al*., 2008; Xue *et al*., 2009), etc.

Precipitation is an important meteorological factor that can influence biological, hydrological, and ecological processes, and thus plays a far-reaching role in the energy balance, water cycle, and sustainability of terrestrial ecosystems. A detailed analysis of precipitation variation in the TRS region is of great significance not only for local ecological protection and sustainable economic development, but also for hydrological processes and agricultural production in the valleys of the lower reaches of the three rivers. Previous studies have shown that precipitation in the TP is closely related to atmospheric circulation, such as the North Atlantic Oscillation (NAO), the Arctic Oscillation, and the westerly jet over East Asia (Ju *et al*., 2005; Yao *et al*., 2012; Gao *et al*., 2013; Wang *et al*., 2018; Bao and You, 2019; He *et al*., 2019). Liu and Yin (2001)

indicated that the variation of the upstream zonal flow related to the NAO is the foremost mechanism that links regional precipitation fluctuation over the TP in summer with large-scale circulation conditions. The interannual variation in summer precipitation is influenced by water vapor transport (WVT). The NAO influences the meridional location of the Asian jet, weakens moisture transport at the western edge of the southern TP region, and eventually induces less precipitation in summer (Wang *et al*., 2017a). The above analyses on the precipitation mechanism all are focused on the TP. The TP is a vast area with complex land surface and different spatial distribution patterns of precipitation. The precipitation trend in the TP demonstrates noticeable regional characteristics (Lin and Zhao, 1996; Wu *et al*., 2007; Guo *et al*., 2018). Therefore, the precipitation mechanism in the TRS region needs further investigation. Some studies have suggested that the TRS region has been experiencing a significant increasing trend of annual precipitation since the 1960s (Liang *et al*., 2013; Yi *et al*., 2013; Shi *et al*., 2016). Recent studies have shown that interannual changes in the springtime precipitation in the TRS region are basically affected by easterly WVT anomalies related to the dominant mode of the Eurasian circulation; moreover, the interannual variability of summer precipitation in the TRS region is largely affected by southwesterly WVT anomalies, which are associated with a wave-train over Eurasia that is connected with the concurrent NAO mode (Sun and Wang, 2018). It is found that the interannual variation in summer precipitation in the TRS region is increasingly closely related to the NAO mode (Sun and Wang, 2019).

However, the atmospheric circulation anomalies associated with the interannual variation of winter precipitation over the TRS region still remain unclear. Snowfall during winter can affect winter climate in the TRS region and Asia via albedo feedback (Qian *et al*., 2003; Shi *et al*., 2011), and also affect the hydrological cycle in the TRS region as well as entire China (Räisänen, 2008; Deng *et al*., 2017). Winter precipitation is kept in the form of snow, and snowpack is a potential source of river runoff in summer and can behave as a buffer zone in the hydrological system to control the flow of rivers (Räisänen, 2008). In addition, snow cover over the TRS region can affect the East Asian

summer monsoon through affecting the transfer of heat from the ground to the atmosphere over the TP (Zhang *et al*., 2004; Xiao and Duan, 2016) and subsequently influences summer precipitation downstream of the TP (Si and Ding, 2013; Wang *et al*., 2017b). Remarkably, the East Asian climate anomalies and related mechanisms can be significantly different in the winter months (He and Wang, 2013; Xu *et al*., 2018a; Sun *et al*., 2019). For example, surface air temperature and circulation anomalies associated with the Siberian high over East Asia are different between November and December–January during 1979–2015 (Lü *et al*., 2019). In December 2014, the cold surface temperature anomalies occurred in East Asia, while the warm anomalies prevailed in January and February 2015 (Xu *et al*., 2018b).

Thus, the present study is focused on the following two issues:

(1) What is the interannual variability of TRS precipitation in different winter months?

(2) What are the mechanisms for the interannual variability of TRS precipitation in different winter months?

The outline of this paper is as follows. Section 2 introduces the data and methods used in this work. The interannual variability of monthly precipitation over the TRS region in winter is discussed in Section 3. Section 4 is focused on the mechanisms for the interannual variability of monthly precipitation in winter over the TRS region. A discussion and summary are provided in Sections 5 and 6, respectively. Supporting information comprises Figures S1–S7.

2. Data and methods

Daily precipitation observational dataset for the period of 1980 to 2015 are provided by the China Meteorological Administration. The dataset consists of observations collected at 50 stations in the TRS region (denoted by red dots in Figure 1). The atmospheric circulation fields are extracted from the ERA-Interim dataset (Dee *et al*., 2011), which has a resolution of 2.0°×2.0°. Variables include the u and v wind components, geopotential height (hereafter Z), vertical velocity, and specific humidity at 23 pressure

levels from 1000 to 200 hPa, 10-meter u and v wind components, surface pressure, and surface latent heat flux. The monthly Niño 3 SST index, the North Atlantic Oscillation (NAO) index, and the Scandinavian index produced by the National Oceanic and Atmospheric Administration (NOAA) Climate Prediction Center are also used (https://www.esrl.noaa.gov/psd/data/climateindices/list/). The Niño 3 index is defined as the areal mean sea surface temperature (SST) over the eastern tropical Pacific (5°N–5°S, 90°–150°W). The NAO and Scandinavian indices are defined as the time series of the first and ninth modes of rotated principal component analysis of Z500 over the Northern Hemisphere (20°–90°N), respectively (http://www.cpc.ncep.noaa.gov/data/teledoc/teleindcalc.shtml). The Scandinavia pattern previously has been referred to as the Eurasia 1 (EU1) pattern by Barnston and Livezey (1987). The monthly SST data used in this study are extracted from the Extended Reconstructed Sea Surface Temperature (ERSST) v5 produced by NOAA. The horizontal resolution of the ERSST is 2.0°×2.0° (Huang *et al*., 2017).

Considering that the snow season in the TRS region mainly spans from November to subsequent March, the winter season in the TRS region is defined as November–March in this study, while early winter is defined as November–December and late winter is defined as January–March. The domain of the TRS region is defined as a rectangular region over (31.5°–36.5°N, 89.5°–102.5°E) denoted by the blue rectangle in Figure 1.

Time series of monthly precipitation averaged over 50 stations in the TRS region in winter are referred to as the time series of TRS precipitation in this study. Linear regression analysis is performed to reveal climatic anomalies associated with the TRS precipitation in this study. In addition, the method of Empirical Orthogonal Function (EOF) analysis is employed to analyze the atmospheric internal processes. The wave activity flux (WAF) indicates wave activity propagation. To avoid confusion, the paper of Takaya and Nakamura (2001) has been cited as the reference for WAF in the manuscript. The algorithm for the calculation of WAF is as follows.

$$\mathbf{W}=\frac{p\cos\phi}{2|\mathbf{U}|}\begin{pmatrix}\frac{U}{a^2\cos^2\phi}\left[\left(\frac{\partial\psi'}{\partial\lambda}\right)^2-\psi'\frac{\partial^2\psi'}{\partial\lambda^2}\right]+\frac{V}{a^2\cos\phi}\left[\frac{\partial\psi'}{\partial\lambda}\frac{\partial\psi'}{\partial\phi}-\psi'\frac{\partial^2\psi'}{\partial\lambda\partial\phi}\right]\\ \frac{U}{a^2\cos\phi}\left[\frac{\partial\psi'}{\partial\lambda}\frac{\partial\psi'}{\partial\phi}-\psi'\frac{\partial^2\psi'}{\partial\lambda\partial\phi}\right]+\frac{V}{a^2}\left[\left(\frac{\partial\psi'}{\partial\phi}\right)^2-\psi'\frac{\partial^2\psi'}{\partial\phi^2}\right]\\ \frac{f_0^2}{N^2}\left\{\frac{U}{a\cos\phi}\left[\frac{\partial\psi'}{\partial\lambda}\frac{\partial\psi'}{\partial z}-\psi'\frac{\partial^2\psi'}{\partial\lambda\partial z}\right]+\frac{V}{a}\left[\frac{\partial\psi'}{\partial\phi}\frac{\partial\psi'}{\partial z}-\psi'\frac{\partial^2\psi'}{\partial\phi\partial z}\right]\right\}\end{pmatrix}+\mathbf{C}_U M \tag{1}$$

In algorithm (1), p = (pressure / 1000hPa); $\mathbf{U} = (U, V, 0)^{\mathrm{T}}$; ϕ denotes the latitude; λ denotes the longitude; a is the average radius of the earth; ψ is the geostrophic streamfunction; $z = -H \ln p$, where H denotes a constant scale height; $N^2=\left(R_\alpha p^k / H\right)(\partial\theta/\partial z)$ is the squared buoyancy frequency, in which R_α is the gas constant of dry air, θ is potential temperature, $k = R / C_p$; $\mathbf{C}_U=\left(\frac{U}{|\mathbf{U}|}C_p,\frac{V}{|\mathbf{U}|}C_p,0\right)^T$ denotes the propagation in the **U** direction; $M=\frac{p}{2}\left(\frac{q'^2}{2|\nabla_H Q|}+\frac{e}{|\mathbf{U}|-C_p}\right)\cos\phi$ denotes the wave-activity pseudo-momentum.

In this study, the Pearson correlation coefficient is calculated to characterize the correlation between time series, and the statistical significance is obtained using Student's *t*-test. To analyze the interannual variation, the linear trends are removed from the data before all analyses.

The water vapor flux crossing the southern, eastern, northern, and western boundaries of the TRS region is calculated using the method developed by Sun et al, (2011). In the present study, the SST tendency index is used to represent the development of ENSO, which is calculated by subtracting the November Niño 3 index from the December Niño 3 index. The dispersion coefficient, which is defined as the ratio of the standard deviation to the mean, is used to compare the dispersion degree of monthly precipitation in winter over the TRS region.

Note that the same analyses have been performed for all the winter months from November to March. In the following sections, only those results associated with the

main mechanisms and factors that influence precipitation over the TRS region during different months in winter are shown and discussed.

To make a clear comparison of the climate anomalies associated with precipitation over the TRS region during different months in winter, all the figures of SST and geopotential height in this paper are plotted over the region within the same latitudinal and longitudinal ranges. For example, the SST anomalies are shown over a spatial range of 20°S–80°N and 180°W–180°E in all the figures.

3. Interannual variability of winter precipitation in the TRS region

The TRS precipitation averages (variances) in November, December, January, February, and March are 3.6 mm (3.1 mm^2), 1.9 mm (1.3 mm^2), 3.1 mm (3.9 mm^2), 4.1 mm (3.1 mm^2), and 9.1 mm (9.7 mm^2), respectively, with the most precipitation in March and the least precipitation in December. The linear trends of TRS precipitation in different months of winter are 0.13 mm $(10\ yr)^{-1}$, -0.33 mm $(10\ yr)^{-1}$, -0.05 mm $(10\ yr)^{-1}$, 0.03 mm $(10\ yr)^{-1}$, and -0.64 mm $(10\ yr)^{-1}$, respectively. The trend of December precipitation is significant at the 95% confidence level. From November to subsequent March, the percentages of total precipitation in winter accounted for by precipitation in individual months are approximately 17%, 9%, 14%, 19%, and 41%, respectively, which increase gradually from December to March (Figure 2a). The interannual variations in the TRS precipitation during different months of winter are significant and fluctuate around their climatic averages from 1980–2015 (Figure 2b–f). The dispersion coefficients of winter precipitation also demonstrate the same feature (Table 1), and the interannual variations of the TRS precipitation in December and January are the most significant (Table 1).

Noticeably, different interannual variations are observed in the time series of TRS precipitation during different months of winter (Figure 2b–f), which is manifested in mostly small correlation coefficients for pairs of randomly combined time series of monthly precipitation during winter (Table 1). For instance, the precipitation was 1.6

mm less than normal (Figure 2b) and 1.3 mm more than normal (Figure 2c) in November and December 1987, respectively; the variations of precipitation anomaly in January and March are in opposite phase during 2001–2005 (Figure 2d, f). These results imply that the interannual variability of TRS precipitation is influenced by different mechanisms during different months of winter.

4. Regimes of the interannual variability of TRS winter precipitation

4.1. Early winter

a) November

Figure 3a shows vertically integrated WVT anomalies regressed on the detrended and standardized time series of TRS precipitation in November. The interannual variation in November precipitation is influenced by anomalous westerly moisture transport over the TRS region. The correlation coefficient between the detrended time series of November precipitation and anomalies of westerly moisture transport is 0.4, which is significant at the 95% confidence level. The anomalous westerly WVT transport is affected by an anomalous cyclone located over the TRS region, which is related to the low pressure anomaly extending from the Middle East to the TP (Figure 3b). The low pressure anomaly is a node of the wave-train over the North Atlantic-Europe-TP (NA-E-TP). This wave-train is characterized by an anomalous low over the North Atlantic, an anomalous high over Europe, and an anomalous low centered in central Asia and extends toward the TP (see Z500 anomalies in Figure 3b). To understand the mechanism of the NA-E-TP wave-train, WAF and divergence of WAF are computed. Significant divergence of WAF can be found in the mid- to high-latitudes of the North Atlantic (Figure 3c), indicating that the NA-E-TP wave-train originates from the mid- to high-latitudes of North Atlantic and propagates eastward (see WAF in Figure 3d). The development and propagation of the NA-E-TP wave-train may be associated with the ocean-atmosphere interaction over the North Atlantic.

In order to better understand the NA-E-TP wave-train, SST anomalies in November are regressed on the detrended and standardized time series of TRS precipitation in

November (Figure 4b). The NA-E-TP wave-train is associated with cold SST anomalies in the mid- to high-latitudes of North Atlantic and warm SST anomalies along the west coast of Europe (Figure 4b). The positive and negative SST anomalies can cause upward and downward motions over the mid- to high-latitude North Atlantic, where anomalous cyclones and anticyclones form (Figure 4a). The anomalous anticyclone (cyclone) strengthens (weakens) westerly winds in the surface of the middle North Atlantic (the western coast of Europe; Figure 4c), resulting in increased (weakened) release of latent heat to the atmosphere over the sea (Figure 4d) and negative (positive) SST anomalies. The ocean-atmosphere interaction can trigger atmospheric circulation anomalies and wave-trains over the Atlantic and Europe, which then propagate eastward and affect the TRS region.

In addition, the present study also found that the SST anomalies over the mid- to high-latitude North Atlantic that are associated with the TRS precipitation may initially occur during September and persist to November (Figure S1 and Figure 4b), and influence the TRS precipitation in November. An understanding of this teleconnection is conducive to a better prediction of the TRS precipitation in November.

In order to understand the internal process of atmospheric variability in November, the leading EOF mode of Z500 over Eurasia (10°–60°N, 20°W–130°E) in November is computed. The correlation coefficient between the detrended time series of the leading EOF mode of Eurasian Z500 and the TRS precipitation in November is 0.11, which is not significant at the 80% confidence level, suggesting that the leading EOF mode of Eurasian Z500 in November has an insignificant influence on the synchronous TRS precipitation.

b) December

The interannual variability of TRS precipitation in December is influenced by an anomalous westerly WVT branch that crosses the western boundary of the TRS region and an anomalous southerly WVT branch that crosses the southern boundary of the TRS region (Figure 5a). The anomalous westerly WVT branch is mainly derived from an anomalous cyclone that is associated with an anomalous low extending from the

Ural Mountains to western Asia, while the anomalous southerly WVT branch is resulted from joint effects of the abovementioned anomalous cyclone and an anomalous anticyclone that is associated with a high pressure anomaly located over Northeast China (Figure 5b). The anomalous high and low correspond to two nodes of a zonal wave-train in the Northern Hemisphere. The circum-global zonal wave-train consists of three anomalous highs and three anomalous lows. The three anomalous highs are centered in North America, the Western Europe, and from Northeast China to the western Pacific coast; the centers of the three anomalous lows are located in the Aleutian Islands, the mid- to high-latitude North Atlantic, and the Ural Mountains (see Z500 anomalies shown in Figure 5b).

Based on Z500 anomalies in the Western Europe (35°–55°N, 0°–25°E), the Ural Mountains (40°–80°N, 40°–90°E) and from Northeast China to the western Pacific coast (35°–50°N, 100°–140°E), as well as that over the Aleutian Islands (45°–70°N, 150°E–150°W), North America (45°–65°N, 80°–120°W) and the mid- to high-latitude North Atlantic (40°–60°N, 30°–60°W), the circum-global teleconnection (CGT) index is defined to further investigate the influence of the circum-global teleconnection on December precipitation in the TRS region. The CGT index is calculated by:

CGT index = Z500 (35°–55°N, 0°–25°E) - Z500 (40°–80°N, 40°–90°E) + Z500 (35°–50°N, 100°–140°E) - Z500 (45°–70°N, 150°E–150°W) + Z500 (45°–65°N, 80°–120°W) - Z500 (40°–60°N, 30°–60°W).

As shown in Figure 5c, WAF of the circum-global zonal wave-train indicates that this wave-train partially originates from the tropical Pacific during December and propagates northeastward towards the North Pacific. Meanwhile, the SST anomalies associated with the TRS precipitation in December exhibit an El Niño pattern in the tropical Pacific (Figure 5d), suggesting that the circum-global zonal wave-train may be partially attributed to ENSO. In addition, the characteristics of the WAF associated with the circum-global zonal wave-train and the linear regression of SST with regard to the CGT index also suggests that the circum-global zonal wave-train partially originates from

the central-eastern tropical Pacific (Figure S2). Previous studies (Hoerling 2001; Toniazzo and Scaife 2006; Zhou *et al*. 2014; Sun *et al*. 2019) have documented that during winter, the atmospheric convective anomalies induced by the central-eastern tropical Pacific SST anomalies can trigger northward-propagating Rossby waves and subsequently influence the circum-global atmospheric teleconnection in the Northern Hemisphere. The results of the present study mentioned above are consistent with results of the previous studies. During the propagation process, the path of the circum-global zonal wave-train splits into two routes over the Western Europe (see the WAF in Figure 5c): a northern route passing the Ural Mountains and a southern route passing the Middle East. The northern and southern routes are merged into one path over Northeast China, and the wave-train continues to propagate eastward along this path (see WAF in Figure 5c).

Moreover, the present study shows that the warm SST anomalies in the central-eastern tropical Pacific that are associated with the TRS precipitation in December may be related to the developing El Nino that can be observed in the preceding summer and autumn (Figure S3). This feature may facilitate prediction of the TRS precipitation in December. It should be noted that the correlation coefficients between the detrended time series of December precipitation over the TRS region and the Niño 3 index in the months of July, August, September, October, and November are 0.26, 0.25, 0.27, 0.37, and 0.27, respectively, which are mostly significant below the 95% confidence level. By contrast, the TRS precipitation in December has a high correlation with synchronous SSTs in the central-eastern tropical Pacific with a correlation coefficient of 0.42 that is significant at the 99% confidence level. The result suggests that the SSTs in the central-eastern tropical Pacific may affect the TRS precipitation in December via synchronous teleconnection.

The calculation shows that the detrended time series of leading EOF mode of Z500 over Eurasia (10°–60°N, 20°W–130°E) in December is significantly correlated with the detrended time series of synchronous TRS precipitation, with a correlation coefficient of 0.46 significant at the 99% confidence level. For December, the Z500 anomalies

associated with the leading EOF mode of Eurasian Z500 exhibit a zonal wave-train pattern (Figure S4b) resembling the circum-global teleconnection (Figure 5b). The anomalous low over the Urals induces an anomalous westerly WVT branch across the western boundary of the TRS region (Figure S4a), while a zonal wave-train originates from the tropical Pacific in response to the warm SST anomalies in the central-eastern tropical Pacific (Figure S4c, d). For December, the influence mechanism of the leading mode of Eurasian Z500 resembles the modulation of the CGT pattern on TRS precipitation. The correlation coefficient between the detrended time series of the leading EOF mode of Eurasian Z500 and the CGT index in December is 0.72, which is significant at the 99% confidence level. Thus, the leading EOF mode of Eurasian Z500 can be considered a component of the CGT pattern.

The above analyses reveal several differences in the mechanisms for the interannual variability of TRS precipitation between November and December, including anomalous SST, atmospheric circulation pattern, wave-train propagation path, and WVT related to synchronous precipitation. The NA-E-TP wave-train can be largely triggered by the ocean-atmosphere interaction over the North Atlantic, influencing the interannual variability of November precipitation over the TRS region via the westerly WVT anomalies crossing the western boundary of the TRS region. However, the interannual variability of TRS precipitation in December is affected by anomalous westerly WVT and southerly WVT, which can be associated with the CGT pattern and anomalous warm SSTs in the tropical Pacific.

4.2. Late winter

a) January and February

The interannual variability of TRS precipitation in January is related to abnormal WVT in the southern boundary of the TRS region (Figure 6a). In January, the correlation coefficient between the detrended time series of TRS precipitation and water vapor flux crossing the southern boundary of the TRS region is 0.68, which is significant at the 99% confidence level. As shown in Figure 6c, the interannual variability of TRS precipitation in January is closely related to an anomalous low over the TRS region and

to its west, which is associated with a northwest-southeast propagating wave-train originating from the mid-latitudes of the North Atlantic and reaching the TRS region (Figure 6e). The wave-train is characterized by an anomalous low centered in the Greenland, an anomalous high centered in the Urals, and an anomalous low centered in the TP (see the Z500 anomalies in Figure 6c). The wave source is located in the mid-latitude North Atlantic, and the wave propagation follows a northern path that passes through West Siberia and a southern path that crosses West Asia (see the WAF in Figure 6e).

The WVT anomalies associated with the TRS precipitation in February are mainly characterized by southwesterly WVT anomalies over the TRS region (Figure 6b). These southwesterly WVT anomalies are induced by an anomalous cyclone that is associated with an anomalous low over the TP (Figure 6d). This anomalous low is related to an anomalous southeastward propagating wave-train (Figure 6f), which is characterized by negative geopotential height anomalies over the Norwegian Sea, positive geopotential height anomalies over the Western Europe, and negative geopotential height anomalies over the TP (see Z500 anomalies in Figure 6d). The wave source is located in the mid-latitudes of the North Atlantic, and the wave propagates eastward across West Asia, reaching the TRS region (see the WAF in Figure 6f). Based on the analysis of the interannual variation in TRS precipitation in November, the spatial distribution of the anomalous high and low centers over the North Atlantic and Europe in January–February is different from that in November. The anomalous high and low centers over the North Atlantic and Europe in January–February are longitudinally distributed and mainly associated with a meridional wave-train (Figure 6e, f), whereas the anomalous centers in November are mainly associated with a zonal wave-train (Figure 3d). In addition, the anomalous low centers affecting the synchronous WVT anomalies are respectively located over the TP (Figure 6c, d) and central Asia (Figure 3b) in January–February and November.

As shown in Figure 6c, d, the anomalous wave-train is associated with a meridional see-saw pattern over the North Atlantic that resembles the positive NAO mode (Trigo *et al*., 2002; Osborn, 2006), and the SST anomalies associated with the TRS

precipitation in January and February exhibit a tripole pattern over the North Atlantic (Fig 6g, h; Pan, 2005; Hurrell and Deser, 2010). Furthermore, different from the mechanism for the interannual variation of the TRS precipitation in December, the interannual variations of the TRS precipitation in January and February are not significantly correlated with the synchronous SST anomalies in the tropical Pacific (Figure 6g, h). Hence, the atmospheric circulation wave-train affecting the TRS precipitation in January and February may be related to a positive NAO mode. The influences of the NAO mode on the interannual variability of TRS precipitation in January and February are explained below.

In January, the Z500 anomalies associated with a positive NAO exhibit a northwest-southeast propagating wave-train over the North Atlantic and Eurasia (see Z500 anomalies in Figure 7c), which resembles the Z500 anomalies associated with the TRS precipitation in January (Figure 6c). The source of the wave-train associated with the January NAO is located in the mid-latitudes of the North Atlantic and the wave propagates southeastward, reaching the TRS region (see WAF in Figure 7c). The abnormal cyclone caused by the anomalous low induces southwesterly WVT anomalies, which cross the southern boundary and enter the TRS region (Figure 7a), leading to increased precipitation there. The influence of the NAO mode in February resembles that in January. Corresponding to the positive phase of NAO (Figure 7b), an anomalous cyclone over the TRS region induces southwesterly WVT anomalies, which cross the southern boundary and enter the TRS region. This abnormal cyclone is induced by an anomalous low, which is attributed to a northwest-southeast propagating wave-train associated with the NAO (see Z500 anomalies in Figure 7d). The source of the wave-train associated with the NAO in February is located in the mid-latitudes of the North Atlantic and the wave propagates southeastward, reaching the TRS region (see WAF in Figure 7d). The increased WTV in the southern boundary of the TRS region leads to precipitation increases over the TRS in February. In addition, Figure 7e shows the detrended and standardized time series of the TRS precipitation and NAO index in January. Their interannual variations are highly consistent, and the correlation coefficient between them

is 0.43, which is significant at the 99% confidence level. The detrended and standardized time series of the TRS precipitation in February and synchronous NAO index also show good consistency (Figure 7f) with a correlation coefficient of 0.38 that is significant at the 95% confidence level. The above analysis suggests that the synchronous NAO is an important factor influencing interannual variation of the TRS precipitation in January and February. The signal associated with January NAO can be observed in the preceding December, which has certain implications for forecasting the TRS precipitation anomalies in January (Figure not shown). However, the early signals associated with February NAO are not found (Figure not shown).

The leading EOF mode of Z500 over Eurasia (10°–60°N, 20°W–130°E) in January and February is also computed. In January, the correlation coefficient between the detrended time series of the leading EOF mode of Eurasian Z500 and TRS precipitation is 0.09, which is not significant at the 80% confidence level. This result suggests that the influence on the synchronous TRS precipitation imposed by the leading EOF mode of Eurasian Z500 in January is not significant. The leading EOF mode of Eurasian Z500 in February causes an anomalous easterly WVT branch, which crosses the eastern boundary and enters the TRS region (Figure S5a). This anomalous easterly WVT branch is related to an abnormal low over Southwest China and an abnormal high over Northeast China (Figure S5b). The correlation coefficient between the detrended time series of the leading EOF mode of Eurasian Z500 in February and synchronous TRS precipitation is 0.29, which is significant at the 90% confidence level. The result suggests that the leading mode of Eurasian Z500 to a certain degree affects interannual variability of the TRS precipitation in February.

b) March

Figure 8a shows anomalies of vertically integrated WVT regressed on the detrended and standardized time series of TRS precipitation in March. The interannual variability of TRS precipitation is closely related to the anomalous southwesterly WVT branch that crosses the southern boundary of the TRS region (Figure 8a). In March, the correlation coefficient of detrended time series of TRS precipitation and water vapor

flux crossing the southern boundary of the TRS region is 0.61, which is significant at the 99% confidence level. This result suggests that the southwesterly WVT anomalies have an important impact on interannual variability of the TRS precipitation in March. The southwesterly WVT anomalies are caused by an anomalous low over the TP that is related to a zonal wave-train in Eurasia (Figure 8b). This wave-train is characterized by high-pressure anomalies over the east coast of North Atlantic, low-pressure anomalies extending from the Eastern Europe to North Africa and the TP, and high-pressure anomalies in Siberia and Northeast China (Figure 8b). It is different from the wave-train over Eurasia that is associated with the TRS precipitation in December (Figure 5b). Unlike their impact on the TRS precipitation in December, the impact of the central-eastern tropical Pacific SST anomalies on interannual variation of the TRS precipitation in March is not significant (Figure S6).

To understand the anomalous zonal wave-train mentioned above, the leading EOF mode of Z500 over Eurasia (10°–60°N, 20°W–130°E) is computed (Figure 8d). The result shows that the leading EOF mode of Eurasian Z500 accounts for 26.9% of the total variance. Its spatial pattern resembles the anomalous Eurasian wave-train that affects the TRS precipitation in March, which is characterized by an anomalous high center over the west coast of Europe, an anomalous low center over north of the Black Sea and the Caspian Sea, and an anomalous high center near the Lake Baikal (Figure 8d). The leading EOF mode of Eurasian Z500 resembles the EU1 pattern. The EU1 consists of a foremost circulation center located over the Scandinavian Peninsula and several other weaker centers located over the Northeast Atlantic Ocean and Siberia (Zhu and Chen, 2019). The detrended time series of the leading EOF mode of Eurasian Z500 is significantly correlated with the detrended EU1 index, and the correlation coefficient is -0.46, which is significant at the 99% confidence level. After detrending and standardization, the time series of the leading EOF mode of Eurasian Z500 shows a good consistency with the time series of the TRS precipitation in March. The correlation coefficient between them is 0.61, which is significant at the 99% confidence level.

(Figure 8c). This result suggests a dominant influence of the leading mode of atmospheric circulation over Eurasia on the interannual variability of TRS precipitation in March.

The WAF and the divergence of the WAF are computed to study the mechanism for the leading EOF mode of Z500 over Eurasia. The significant divergence of the WAF over the mid-latitude North Atlantic (Figure 9a) suggests that the wave-train associated with the leading EOF mode of Eurasian Z500 originates from the west of the North Atlantic (see WAF in Figure 9b), which may be related to the ocean-atmosphere interaction over the North Atlantic. Warm SST anomalies in the west of North Atlantic associated with the leading EOF mode of Eurasian Z500 (Figure 9d) can contribute to abnormal ascending motions (Figure 9c), resulting in strengthened convection over the west of the North Atlantic and triggering the wave-train over Eurasia (see Z200 anomalies in Figure 9b).

For the preceding February, the Z500 anomalies associated with March precipitation over the TRS region resemble a positive NAO mode over North Atlantic (Figure S7), and the correlation coefficient between the time series of March precipitation over the TRS region and February NAO index is 0.22, which is significant at the 80% confidence level. This suggests that the zonal wave-train associated with the TRS precipitation in March may partially stem from a positive NAO mode during the preceding February, which also is a possible reason for the high correlation between interannual variations of the TRS precipitation in February and March (Table 1).

The above analysis reveals different mechanisms for the interannual variability of TRS precipitation in January, February, and March. The interannual variations of the TRS precipitation in January and February are influenced by the synchronous NAO, whereas the interannual variation of TRS precipitation in March is influenced by the leading mode of Eurasian Z500. Although the precipitation in January and February are influenced by the NAO, the paths of the wave-trains associated with the NAO are different between January and February, i.e., two separate paths are found in January and only one path is found in February.

5. Discussion

Two questions arise from the above results: (1) considering that the NAO is a key influencing factor for the concurrent precipitation over the TRS region during January and February, why are the time series of precipitation during January and February insignificantly correlated (Table 1)? (2) the mechanisms for the interannual variability of precipitation during November and December are different, why are the time series of precipitation during November and December significantly correlated (Table 1)?

For the first question, the possible answer is that although the precipitation during January and February over the TRS region is primarily modulated by synchronous NAO, there are differences in the variation of NAO between different months of winter (Watanabe, 2004; Hurrell and Deser, 2010). The correlation coefficient between the detrended NAO indexes in January and February is 0.26, which is not significant at the 90% confidence level, indicating an insignificant relationship between the NAO in January and February. Therefore, there is an insignificant correlation between the TRS precipitation in January and February.

For the second question, previous studies have shown that ENSO in its developing stage has an important impact on the climate of East Asia (Wu *et al*., 2003; Chen *et al*., 2012; Lee *et al*., 2013; Luo and Wang, 2017). Thus, the significant correlation between the TRS precipitation in November and December may be linked to the developing ENSO. To verify this point, the anomalies of Z500 and SST in November and December are regressed onto the detrended and standardized SST tendency index (subtract the November Niño 3 index from the December Niño 3 index). Results are displayed in Figure 10, which shows that the anomalies of Z500 and SST associated with the SST tendency in November (Figure 10a, b) and December (Figure 10c, d) are respectively similar to the anomalies of Z500 and SST associated with the TRS precipitation in November (Figure 3b and Figure 4b) and December (Figure 5b, d). In addition, there is a significant correlation between the time series of November/December precipitation over the TRS region and SST tendency index. The correlation coefficients are 0.38 and 0.34 for November and December, respectively, and both are significant at the 95%

confidence level. These results indicate that the TRS precipitation in November and December is related to ENSO in its developing stage. Consequently, there is a significant correlation between time series of the TRS precipitation in November and December.

6. Summary

In this study, the interannual variation in precipitation over the TRS region and the mechanisms for the variation are analyzed for different months of winter over the period of 1980–2015. Different interannual variations are observed in monthly precipitation from November to March, which can be attributed to different mechanisms.

The interannual variations of the TRS precipitation in November and December are mainly affected by an anomalous westerly WVT branch that crosses the western boundary of the TRS region, whereas the interannual variations of the TRS precipitation in January, February, and March are mainly affected by an anomalous southwesterly WVT branch that crosses the southern boundary of the TRS region.

In November, SST anomalies in the mid- to high-latitudes of the North Atlantic can trigger a NA-E-TP wave-train via the ocean-atmosphere interaction, which subsequently induces an anomalous low over the TRS region. The anomalous low causes westerly WVT anomalies and modulates the interannual variation of precipitation over the TRS region. The interannual variation of the TRS precipitation in December is mainly modulated by the CGT pattern associated with warm SST anomalies in the central-eastern tropical Pacific. During its propagation, the path of the CGT wave-train splits into two separate paths in the Western Europe, and the two paths merge in northeast China to form a single path again. The mechanisms for the interannual variations of the TRS precipitation in January and February are similar, which are mainly under the influence of the synchronous NAO. However, the propagation paths of the wave-train associated with the TRS precipitation are different in January and February. The

wave-train propagates via two paths in January, whereas it follows a single path in February. The interannual variation of precipitation in March is modulated by the leading EOF mode of Eurasian Z500 that resembles the EU1 pattern.

The above analysis shows that the main factors associated with the interannual variation of monthly precipitation over the TRS region are different in winter (Table 2), which is the reasons why the interannual variation of monthly precipitation over the TRS region is different in individual winter months.

Acknowledgements

This study is funded by the National Natural Science Foundation of China (Grant Nos. 41991283 and 41805047), the Natural Science Foundation of Jiangsu Province of China (Grant No. BK20180807), and the Jiangsu Innovation & Entrepreneurship Team.

Supporting information

SST anomalies in September and October associated with the TRS precipitation in November are shown in Figure S1; Z200 anomalies, SST anomalies, and WAF associated with the circum-global teleconnection (CGT) index in December are shown in Figure S2; SST anomalies during July–November associated with the TRS precipitation in December are shown in Figure S3; WVT anomalies, Z200 anomalies, SST anomalies, and WAF associated with the leading EOF mode of Eurasian Z500 in December are shown in Figure S4; WVT anomalies and Z500 anomalies associated with the leading EOF mode of Eurasian Z500 in February are shown in Figure S5; SST anomalies in March associated with synchronous TRS precipitation are shown in Figure S6; Z500 anomalies in February associated with the TRS precipitation in March are shown in Figure S7.

References

Bao YT, You QL (2019) How do westerly jet streams regulate the winter snow depth over the Tibetan Plateau? *Climate Dynamics*, 53, 353–370. https://doi.org/10.1007/s00382-018-4589-1.

Barnston AG, Livezey RE (1987) Classification, Seasonality and Persistence of Low-Frequency Atmospheric Circulation Patterns. *Monthly Weather Review*, 115(6), 1083-1126.

Chen Y, Zhao Y, Feng J, Wang, F (2012) ENSO cycle and climate anomaly in China. Chinese Journal of Oceanology and Limnology, 30, 985-1000.

Dee DP, Uppala SM, Simmons AJ, Berrisford P, Poli P, Kobayashi S, Andrae U, Balmaseda MA, Balsamo G, Bauer P, Bechtold P, Beljaars ACM, van de Berg L, Bidlot J, Bormann N, Delsol C, Dragani R, Fuentes M, Geer AJ, Haimberger L, Healy SB, Hersbach H, Hólm E V., Isaksen L, Kållberg P, Köhler M, Matricardi M, McNally AP, Monge-Sanz BM, Morcrette J-J, Park B-K, Peubey C, de Rosnay P, Tavolato C, Thépaut J-N, Vitart F (2011) The ERA-Interim reanalysis: configuration and performance of the data assimilation system. *Quarterly Journal of the Royal Meteorological Society*, 137, 553–597. https://doi.org/10.1002/qj.828.

Deng HJ, Pepin NC, Chen YM (2017) Changes of snowfall under warming in the Tibetan Plateau. *Journal of Geophysical Research*, 122, 7323–7341. https://doi.org/10.1002/2017JD026524.

He C, Wang ZQ, Zhou TJ, Li T (2019) Enhanced latent heating over the Tibetan Plateau as a key to the enhanced East asian summer monsoon circulation under a warming climate. *Journal of Climate*, 32, 3373–3388. https://doi.org/10.1175/JCLI-D-18-0427.1.

He SP, Wang HJ (2013) Impact of the November/December Arctic Oscillation on the following January temperature in East Asia. *Journal of Geophysical Research Atmospheres*, 118, 12981–12998. https://doi.org/10.1002/2013JD020525.

Hoerling MP (2001) Tropical Origins for Recent North Atlantic Climate Change. Science, 292, 90–92. https://doi.org/10.1126/science.1058582.

Huang BY, Thorne PW, Banzon VF, Boyer T, Chepurin G, Lawrimore JH, Menne MJ, Smith TM, Vose RS, Zhang HM (2017) Extended Reconstructed Sea Surface Temperature, Version 5 (ERSSTv5): Upgrades, Validations, and Intercomparisons. *Journal of Climate*, 30, 8179–8205. https://doi.org/10.1175/JCLI-D-16-0836.1.

Hurrell JW, Deser C (2010) North Atlantic climate variability: The role of the North Atlantic Oscillation. *Journal of Marine Systems*, 79, 231–244. https://doi.org/10.1016/j.jmarsys.2009.11.002.

Hu YR, Maskey S, Uhlenbrook S (2013) Downscaling daily precipitation over the Yellow River source region in China: A comparison of three statistical downscaling methods. *Theoretical and Applied Climatology*, 112, 447–460. https://doi.org/10.1007/s00704-012-0745-4.

Immerzeel WW, Van Beek LPH, Bierkens MFP (2010) Climate Change Will Affect the Asian Water Towers. Science, 328, 1382–1385. https://doi.org/10.1126/science.1183188.

Jiang C, Zhang LB (2015) Climate Change and Its Impact on the Eco-Environment of the Three-Rivers Headwater Region on the Tibetan Plateau, China. *International Journal of Environmental Research and Public Health*, 12, 12057–12081. https://doi.org/10.3390/ijerph121012057.

Jiang C, Zhang LB (2016) Effect of ecological restoration and climate change on ecosystems: a case study in the Three-Rivers Headwater Region, China.

Environmental Monitoring and Assessment, 188, 382. https://doi.org/10.1007/s10661-016-5368-2.

Jiang XW, Li YQ, Yang S, Yang K, Chen JW (2016) Interannual variation of summer atmospheric heat source over the Tibetan Plateau and the role of convection around the Western Maritime Continent. *Journal of Climate*, 29, 121–138. https://doi.org/10.1175/JCLI-D-15-0181.1.

Ju JH, Lü JM, Cao J, Ren JZ (2005) Possible impacts of the Arctic Oscillation on the interdecadal variation of summer monsoon rainfall in East Asia. *Advances in Atmospheric Sciences*, 22, 39–48.

Lee J, Lee S, Wang B, Ha K, Jhun J (2013) Seasonal prediction and predictability of the Asian winter temperature variability. *Climate Dynamics*, 41, 573-587.

Liang LQ, Li LJ, Liu CM, Cuo L (2013) Climate change in the Tibetan Plateau Three Rivers Source Region: 1960-2009. *International Journal of Climatology*, 33, 2900–2916. https://doi.org/10.1002/joc.3642.

Lin ZY, Zhao XY (1996) Spatial characteristics of changes in temperature and precipi tation of the Qinghai-Xizang (Tibet) Plateau. *Science in China, Series D: Earth Sciences*, 39, 442–448. https://doi.org/10.1360/yd1996-39-4-442.

Liu J, Milne RI, Cadotte MW, Wu ZY, Provan J, Zhu GF, Gao LM, Li DZ (2018) Protect Third Pole's fragile ecosystem. *Science*, 362, 1368. https://doi.org/10.1126/science.aaw0443.

Liu JY, Xu XL, Shao QQ (2008) Grassland degradation in the "Three-River Headwaters" region, Qinghai Province. *Journal of Geographical Sciences*, 18, 259–273. https://doi.org/10.1007/s11442-008-0259-2.

Liu XD, Yin ZY (2001) Spatial and Temporal Variation of Summer Precipitation over the Eastern Tibetan Plateau and the North Atlantic Oscillation. *Journal of Climate*, 14, 2896–2909. https://doi.org/10.1175/1520-0442(2001)014<2896:SATVOS>2.0.CO;2.

Luo X, Wang B (2017) How predictable is the winter extremely cold days over temperate East Asia. *Climate Dynamics*, 48, 2557-2568.

Lü ZZ, He SP, Li F, Wang HJ (2019) Impacts of the Autumn Arctic Sea Ice on the Intraseasonal Reversal of the Winter Siberian High. *Advances in Atmospheric Sciences*, 36, 173–188. https://doi.org/10.1007/s00376-017-8089-8.Osborn TJ (2006) Recent variations in the winter North Atlantic oscillation. *Weather*, 61, 353–355. https://doi.org/10.1256/wea.190.06.

Pan LL (2005) Observed positive feedback between the NAO and the North Atlantic SSTA tripole. *Geophysical Research Letters*, 32, L06707. https://doi.org/10.1029/2005GL022427.

Qian YF, Zheng YQ, Zhang Y, Miao MQ (2003) Responses of China's summer monsoon climate to snow anomaly over the Tibetan Plateau. *International Journal of Climatology*, 23, 593–613. https://doi.org/10.1002/joc.901.

Räisänen J (2008) Warmer climate: Less or more snow? *Climate Dynamics*, 30, 307–319. https://doi.org/10.1007/s00382-007-0289-y.

Shi HY, Li TJ, Wei JH, Wang F, Wang GQ (2016) Spatial and temporal characteristics of precipitation over the Three-River Headwaters region during 1961-2014. *Journal of Hydrology: Regional Studies*, 6, 52–65. https://doi.org/10.1016/j.ejrh.2016.03.001.

Shi Y, Gao XJ, Wu J, Giorgi F (2011) Changes in snow cover over China in the 21st century as simulated by a high resolution regional climate model. *Environmental Research Letters*, 6, 045401.

Si D, Ding YH (2013) Decadal change in the correlation pattern between the tibetan plateau winter snow and the East Asian summer precipitation during 1979-2011. *Journal of Climate*, 26, 7622–7634. https://doi.org/10.1175/JCLI-D-12-00587.1.

Su FG, Duan XL, Chen DL, Hao ZC, Cuo L (2013) Evaluation of the global climate models in the CMIP5 over the Tibetan Plateau. *Journal of Climate*, 26, 3187–3208. https://doi.org/10.1175/JCLI-D-12-00321.1.

Sun B, Wang HJ (2018) Interannual variation of the spring and summer precipitation over the three river source region in China and the associated regimes. *Journal of Climate*, 31, 7441–7457. https://doi.org/10.1175/JCLI-D-17-0680.1.

Sun B, Wang HJ (2019) Enhanced connections between summer precipitation over the Three-River-Source region of China and the global climate system. *Climate Dynamics*, 52, 3471–3488. https://doi.org/10.1007/s00382-018-4326-9.

Sun B, Zhu YL, Wang HJ (2011) The recent interdecadal and interannual variation of water vapor transport over eastern China. *Advances in Atmospheric Sciences*, 28, 1039–1048. https://doi.org/10.1007/s00376-010-0093-1.

Sun B, Wang HJ, Zhou BT (2019) Interdecadal Variation of the Relationship between East Asian Water Vapor Transport and Tropical Pacific Sea Surface Temperatures during January and Associated Mechanisms. *Journal of Climate*, 7575–7594. https://doi.org/10.1175/jcli-d-19-0290.1.

Sun C, Xiao ZN, Sun JQ, YU ET (2019) Projection of temperature change and extreme temperature events in the Lancang–Mekong River basin. Atmospheric and Oceanic Science Letters, 13, 16–25. https://doi.org/10.1080/16742834.2020.1696143.

Takaya K, Nakamura H (2001) A Formulation of a Phase-Independent Wave-Activity Flux for Stationary and Migratory Quasigeostrophic Eddies on a Zonally Varying Basic Flow. *Journal of the Atmospheric Sciences*, 58, 608–627. https://doi.org/10.1175/1520-0469(2001)058<0608:AFOAPI>2.0.CO;2.

Tong K, Su FG, Yang DQ, Zhang LL, Hao ZC (2014) Tibetan Plateau precipitation as depicted by gauge observations, reanalyses and satellite retrievals. *International Journal of Climatology*, 34, 265–285. https://doi.org/10.1002/joc.3682.

Toniazzo T, Scaife AA (2006) The influence of ENSO on winter North Atlantic climate. *Geophysical Research Letters*, 33, L24704. https://doi.org/10.1029/2006GL027881.

Trigo RM, Osborn TJ, Corte-Real JM (2002) The North Atlantic Oscillation influence on Europe: climate impacts and associated physical mechanisms. *Climate Research*, 20, 9–17. https://doi.org/10.3354/cr020009.

Wang CH, Yang K, Li YL, Wu D, Bo Y (2017b): Impacts of Spatiotemporal Anomalies of Tibetan Plateau Snow Cover on Summer Precipitation in Eastern China.*Journal of Climate*, 30, 885–903. https://doi.org/10.1175/JCLI-D-16-0041.1.

Wang MR, Wang J, Duan AM, Liu YM, Zhou SW (2018) Coupling of the Quasi-Biweekly Oscillation of the Tibetan Plateau Summer Monsoon With the Arctic Oscillation. *Geophysical Research Letters*, 45, 7756–7764. https://doi.org/10.1029/2018GL077136.

Wang ZQ, Duan AM, Yang S, Ullah K (2017a) Atmospheric moisture budget and its regulation on the variability of summer precipitation over the Tibetan Plateau. *Journal of Geophysical Research: Atmospheres*, 122, 614–630. https://doi.org/10.1002/2016JD025515.

Watanabe M (2004) Asian Jet Waveguide and a Downstream Extension of the North Atlantic Oscillation. Journal of Climate, 17, 4674-4691.

Wu R, Hu ZZ, Kirtman BP (2003) Evolution of ENSO-Related Rainfall Anomalies in East Asia. Journal of Climate, 16, 3742-3758.

Wu SH, Yin YH, Zheng D, Yang QY (2007) Climatic trends over the Tibetan Plateau during 1971-2000. *Journal of Geographical Sciences*, 17, 141–151. https://doi.org/10.1007/s11442-007-0141-7.

Xiao ZX, Duan AM (2016) Impacts of Tibetan Plateau snow cover on the interannual variability of the East Asian summer monsoon. *Journal of Climate*, 29, 8495–8514. https://doi.org/10.1175/JCLI-D-16-0029.1.

Xu XP, He SP, Li F, Wang HJ (2018a): Impact of northern Eurasian snow cover in autumn on the warm Arctic–cold Eurasia pattern during the following January and its linkage to stationary planetary waves. *Climate Dynamics*, 50, 1993–2006. https://doi.org/10.1007/s00382-017-3732-8.

Xu XP, Li F, He SP, Wang HJ (2018b) Subseasonal Reversal of East Asian Surface Temperature Variability in Winter 2014/15. *Advances in Atmospheric Sciences*, 35, 737–752. https://doi.org/10.1007/s00376-017-7059-5.

Gao Y, Wang HJ, Li SL (2013) Influences of the Atlantic Ocean on the summer precipitation of the southeastern Tibetan Plateau. *Journal of Geophysical Research Atmospheres*, 118, 3534–3544. https://doi.org/10.1002/jgrd.502902013.

Guo DL, Sun JQ, Yu ET (2018) Evaluation of CORDEX regional climate models in simulating temperature and precipitation over the Tibetan Plateau. Atmospheric and Oceanic Science Letters, 11, 219–227. https://doi.org/10.1080/16742834.2018.1451725.

Yao TD, Thompson L, Yang W, Yu WS, Gao Y, Guo XJ, Yang XX, Duan KQ, Zhao HB, Xu BQ, Pu JC, Lu AX, Xiang Y, Kattel DB, Joswiak D (2012) Different glacier status with atmospheric circulations in Tibetan Plateau and surroundings. *Nature Climate Change*, 2, 663–667. https://doi.org/10.1038/nclimate1580.

Yi XS, Li GS, Yin Y. Y (2013) Spatio-temporal variation of precipitation in the Three-River Headwater Region from 1961 to 2010. *Journal of Geographical Sciences*, 23, 447–464. https://doi.org/10.1007/s11442-013-1021-y.

Zhang YS, Li T, Wang B (2004) Decadal change of the spring snow depth over the Tibetan Plateau: The associated circulation and influence on the East Asian summer monsoon. *Journal of Climate*, 17, 2780–2793. https://doi.org/10.1175/1520-0442(2004)017<2780:DCOTSS>2.0.CO;2.

Zhang Y, Wang GX, Wang YB (2011) Changes in alpine wetland ecosystems of the Qinghai-Tibetan plateau from 1967 to 2004. *Environmental Monitoring and Assessment*, 180, 189–199. https://doi.org/10.1007/s10661-010-1781-0.

Zhou ZQ, Xie SP, Zheng XT, Liu QY, Wang H (2014) Global warming-induced changes in El Niño teleconnections over the North Pacific and North America. *Journal of Climate*, 27, 9050–9064. https://doi.org/10.1175/JCLI-D-14-00254.1.

Zhu L, Chen HS (2019) Possible connection between anomalous activity of Scandinavian Atmospheric Teleconnection Pattern and winter snowfall in the Yangtze-Huaihe River Basin of China. *Atmospheric and Oceanic Science Letters*, 12, 218–225. https://doi.org/10.1080/16742834.2019.1593041.

Figure captions

TABLE 1 Correlation coefficient of TRS precipitation during different months in winterfrom November to March, dispersion coefficient (DC), and Variance.

TABLE 2 Correlation coefficients between the detrended time series of TRS precipitation (Pr) and time series of the leading EOF mode of Z500 over Eurasia (EOF1; 10°–60°N, 20°W–130°E), NAO index, Niño 3 index in November, December, January, February, and March, correspondingly.

FIGURE 1 Topography of the TRS area (color shading; unit: m). The blue rectangle (31.5°–36.5°N, 89.5°–102.5°E) represents the scope of the TRS area. Red dots denote the locations of stations used in this study.

FIGURE 2 (a) Climatological monthly mean precipitation (unit: mm) based on all stations over the TRS region during 1980–2015. Time series of monthly precipitation anomalies (unit: mm) averaged over the TRS region in (b) November, (c) December, (d) January, (e) February, and (f) March with respect to the base period of 1980/81–2014/15.

FIGURE 3 Anomalies of (a) vertically integrated WVT (unit: kg m^{-1} s^{-1}), (b) 500-hPa geopotential height (Z500, unit: gpm), (d) 200-hPa geopotential height (Z200, colored shading, unit: gpm) regressed on the detrended and standardized time series of TRS precipitation in November, (c) divergence of wave activity flux (DWAF, unit: 10^5 m s^{-2}). Vectors in (d) represent wave activity flux (WAF, unit: m^2 s^{-2}) associated with Z200 anomalies. Dark-gray and light-gray shadings represent the

significance level at 90% and 80% confidence levels, respectively. Stippling in (b) and red contour lines in (d) denote the 90% confidence level using Student's *t*-test.

FIGURE 4 Anomalies of (a) 10-meter wind (sfcwind, unit: m s^{-1}), (b) SST (unit: 10 ℃), (d) surface latent heat flux (slhf, unit: W m^{-2}, positive denote upward) regressed on the detrended and standardized time series of TRS precipitation in November, (c) climatology of 10-meter wind (sfcwind climatology, unit: m s^{-1}) in November during 1980–2014. Gray shading in (a) and stippling in (b, d) represent the significance level at the 90% confidence level using Student's *t*-test.

FIGURE 5 Anomalies of (a) vertically integrated WVT (unit: kg m^{-1} s^{-1}), (b) Z500 (unit: gpm), (c) Z200 (colored shading, unit: gpm), (d) SST (unit: 10 ℃) regressed on the detrended and standardized time series of TRS precipitation in December. Vectors in (c) represent the WAF (unit: m^2 s^{-2}) associated with Z200 anomalies. Dark-gray and light-gray shadings in (a) represent the significance level at 90% and 80% confidence levels, respectively. Stippling in (b, d) and red contour lines in (c) denote the 90% confidence level using Student's *t*-test.

FIGURE 6 Anomalies of (a, b) vertically integrated WVT (unit: kg m^{-1} s^{-1}), (c, d) Z500 (unit: gpm), (e, f) Z200 (colored shading, unit: gpm), (g, h) SST (unit: 10 ℃) regressed on the detrended and standardized time series of TRS precipitation in (a, c, e, g) January and (b, d, f, h) February. Vectors in (e, f) represent the WAF (unit: m^2 s^{-2}) associated with Z200 anomalies in (e) January and (f) February. Dark-gray and light-gray shadings in (a, b) represent the significance level at 90% and 80% confidence levels, respectively. Stippling in (c–h) and red contour lines in (e, f) denote the 90% confidence level using Student's *t*-test.

FIGURE 7 Anomalies of (a, b) vertically integrated WVT (unit: kg m^{-1} s^{-1}), (c, d) Z500 (colored shading, unit: gpm) regressed on the detrended and standardized NAO index in (a, c) January and (b, d) February, (e, f) shows detrended and standardized time series of TRS precipitation (Pr; red) and NAO index (blue) in (e) January and (f) February, with the correlation coefficient labeled in the top-right corner. Vectors in (c, d) represent the WAF (unit: m^2 s^{-2}) associated with Z500 anomalies in (c)

January and (d) February. Gray shadings in (a, b) and stippling in (c, d) denote the 90% confidence level using Student's *t*-test.

FIGURE 8 Anomalies of (a) vertically integrated WVT (unit: kg m^{-1} s^{-1}), (b) Z500 (unit: gpm) regressed on the detrended and standardized time series of TRS precipitation in March, (c) shows the detrended and standardized time series of TRS precipitation (Pr; red) and time series of the leading EOF mode of Z500 over Eurasia (EOF1; 10°–60°N, 20°W–130°E; blue) in March, with the correlation coefficient labeled in the top-right corner, (d) Leading EOF mode of Z500 over Eurasia (10°–60°N, 20°W–130°E) in March, with the explained variance labeled in the top-right corner. Dark-gray and light-gray shadings in (a) represent the significance level at 90% and 80% confidence levels, respectively. Stippling in (b) denotes the 90% confidence level using Student's *t*-test.

FIGURE 9 (a) Divergence of wave activity flux (DWAF, unit: 10^5 m s^{-2}), anomalies of (b) Z200 (colored shading, unit: gpm), (c) 500-hPa vertical velocity (ω500, unit: 10^2 Pa s^{-1}, negative values represent upward motion and vice versa), (d) SST (unit: 10 ℃) regressed on the detrended and standardized time series of the leading EOF mode of Z500 over Eurasia (EOF1; 10°–60°N, 20°W–130°E) in March. Vectors in (b) represent the WAF (unit: m^2 s^{-2}) associated with Z200 anomalies. Stippling in (c, d) and red contour lines in (b) denote the 90% confidence level using Student's *t*-test.

FIGURE 10 Anomalies of (a, c) Z500 (unit: gpm), (b, d) SST (unit: 10 ℃) in (a, b) November and (c, d) December regressed on the detrended and standardized time series of the SST tendency (SSTTE) index (subtract the November Niño 3 index from the December Niño 3 index). Stippling denotes the 90% confidence level using the Student's *t*-test.

	Nov	Dec	Jan	Feb	Mar	DC	Variance
Nov	1	0.43**	-0.17	0.16	0.27	0.49	3.1
Dec		1	-0.09	0.13	0.05	0.6	1.3
Jan			1	0.14	0.12	0.63	3.9
Feb				1	0.59**	0.42	3.1
Mar					1	0.34	9.7

Note: ** represent correlation coefficient the significance level at 99%

TABLE 1 Correlation coefficient of TRS precipitation during different months in winter from November to March, dispersion coefficient (DC), and Variance.

	Pr (Nov)	Pr (Dec)	Pr (Jan)	Pr (Feb)	Pr (Mar)
EOF1	0.11	0.46**	0.09	0.29	0.61**
NAO	-0.04	0.05	0.43**	0.38*	0.13
Niño 3	0.13	0.42**	-0.11	-0.08	0.14

Note: *, ** represent correlation coefficient the significance level at 95%, 99%,

TABLE 2 Correlation coefficients between the detrended time series of TRS precipitation (Pr) and time series of the leading EOF mode of Z500 over Eurasia (EOF1; 10°–60°N, 20°W–130°E), NAO index, Niño 3 index in November, December, January, February, and March, correspondingly.

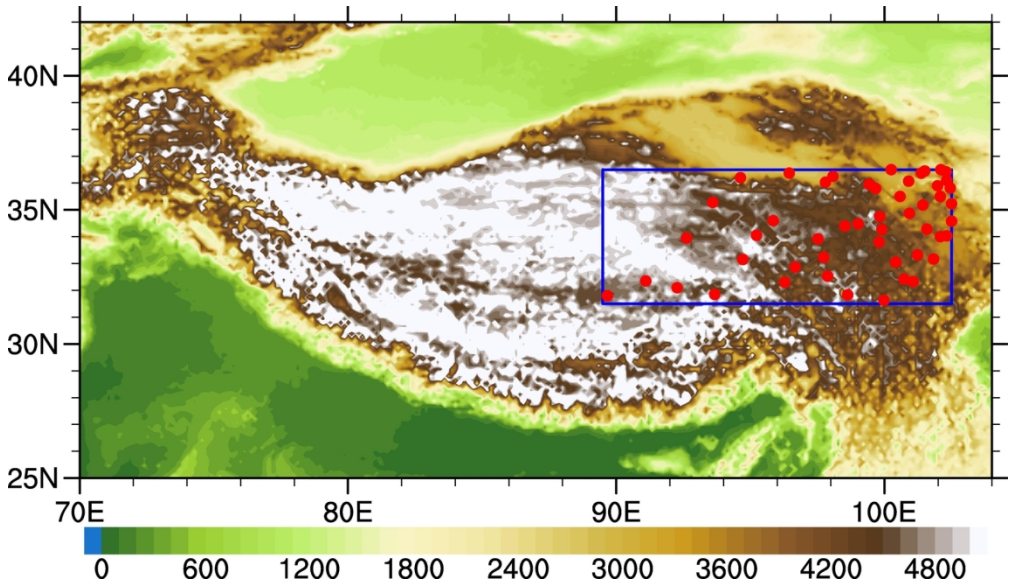

FIGURE 1 Topography of the TRS area (color shading; unit: m). The blue rectangle (31.5°–36.5°N, 89.5°–102.5°E) represents the scope of the TRS area. Red dots denote the locations of stations used in this study.

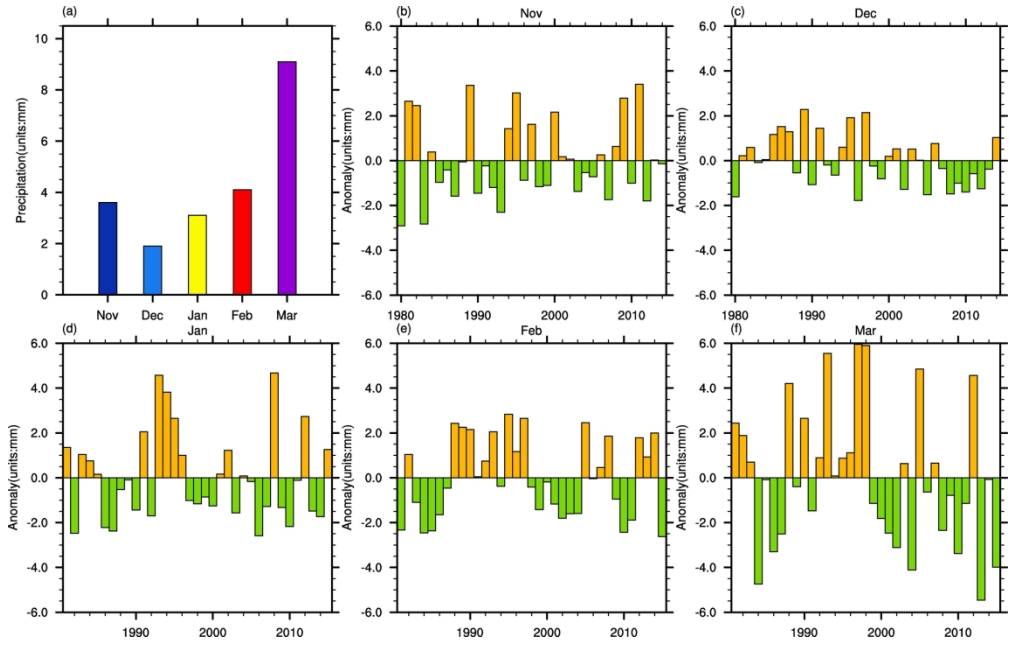

FIGURE 2 (a) Climatological monthly mean precipitation (unit: mm) based on all stations over the TRS region during 1980–2015. Time series of monthly precipitation anomalies (unit: mm) averaged over the TRS region in (b) November, (c) December, (d) January, (e) February, and (f) March with respect to the base period of 1980/81–2014/15.

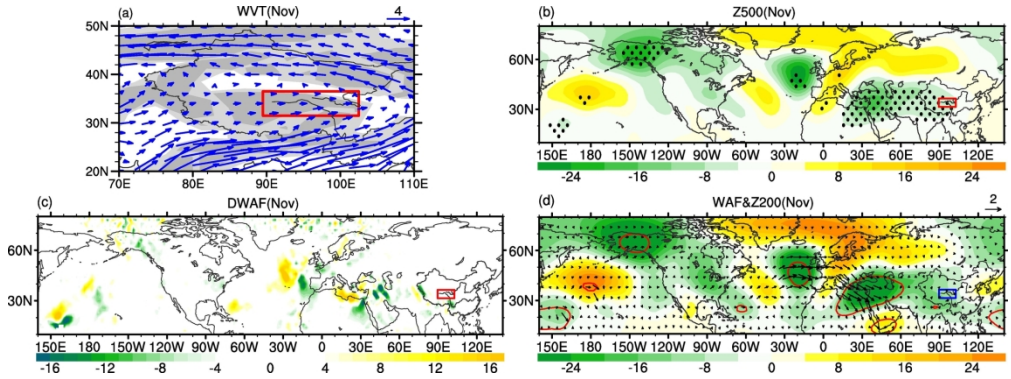

FIGURE 3 Anomalies of (a) vertically integrated WVT (unit: kg m^{-1} s^{-1}), (b) 500-hPa geopotential height (Z500, unit: gpm), (d) 200-hPa geopotential height (Z200, colored shading, unit: gpm) regressed on the detrended and standardized time series of TRS precipitation in November, (c) divergence of wave activity flux (DWAF, unit: 10^5 m s^{-2}). Vectors in (d) represent wave activity flux (WAF, unit: m^2 s^{-2}) associated with Z200 anomalies. Dark-gray and light-gray shadings represent the significance level at 90% and 80% confidence levels, respectively. Stippling in (b) and red contour lines in (d) denote the 90% confidence level using Student's *t*-test.

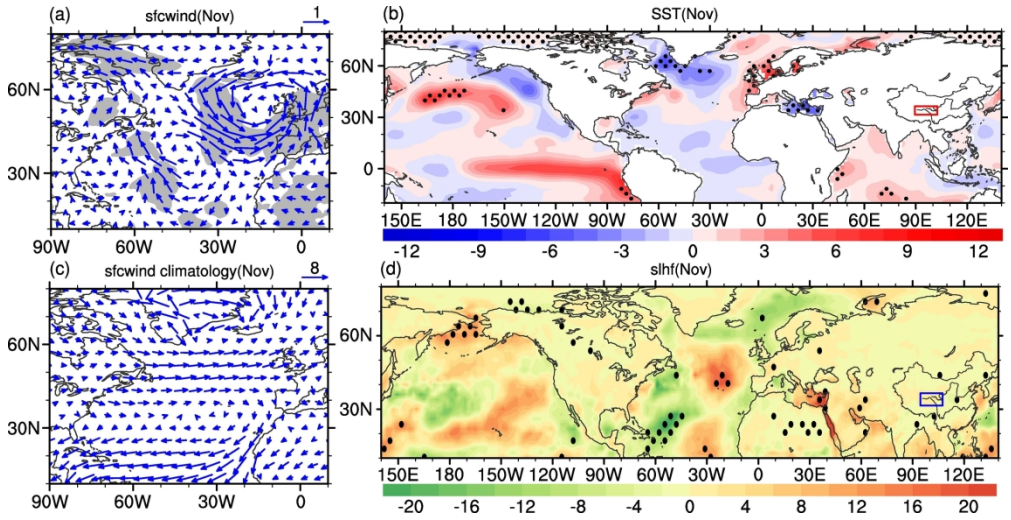

FIGURE 4 Anomalies of (a) 10-meter wind (sfcwind, unit: m s^{-1}), (b) SST (unit: 10 ℃), (d) surface latent heat flux (slhf, unit: W m^{-2}, positive denote upward) regressed on the detrended and standardized time series of TRS precipitation in November, (c) climatology of 10-meter wind (sfcwind climatology, unit: m s^{-1}) in November during 1980–2014. Gray shading in (a) and stippling in (b, d) represent the significance level at the 90% confidence level using Student's *t*-test.

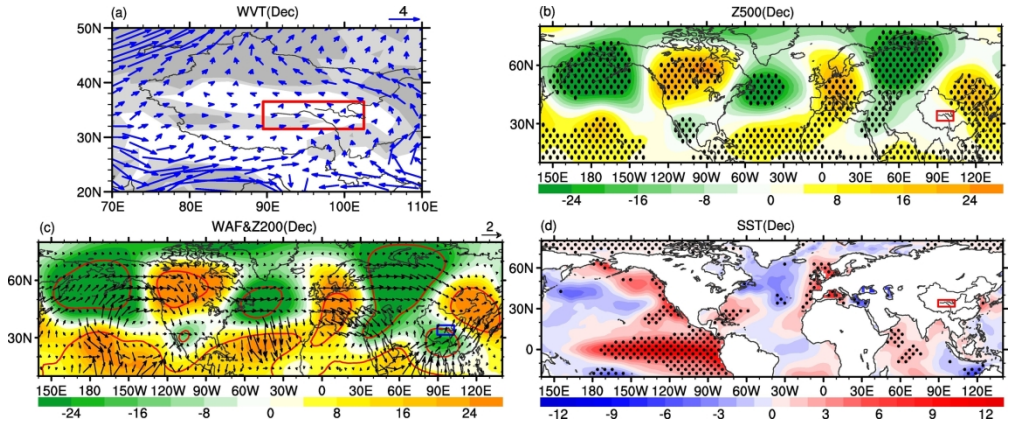

FIGURE 5 Anomalies of (a) vertically integrated WVT (unit: kg m^{-1} s^{-1}), (b) Z500 (unit: gpm), (c) Z200 (colored shading, unit: gpm), (d) SST (unit: 10 ℃) regressed on the detrended and standardized time series of TRS precipitation in December. Vectors in (c) represent the WAF (unit: m^2 s^{-2}) associated with Z200 anomalies. Dark-gray and light-gray shadings in (a) represent the significance level at 90% and 80% confidence levels, respectively. Stippling in (b, d) and red contour lines in (c) denote the 90% confidence level using Student's *t*-test.

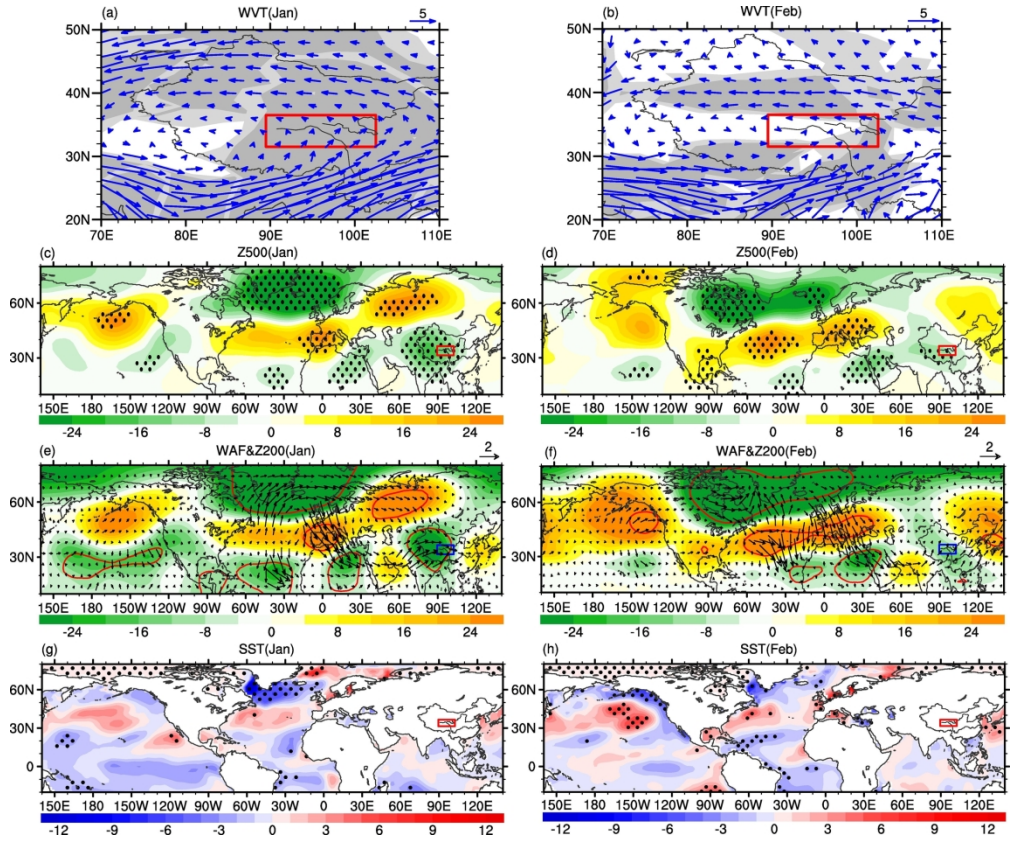

FIGURE 6 Anomalies of (a, b) vertically integrated WVT (unit: kg m^{-1} s^{-1}), (c, d) Z500 (unit: gpm), (e, f) Z200 (colored shading, unit: gpm), (g, h) SST (unit: 10 ℃) regressed on the detrended and standardized time series of TRS precipitation in (a, c, e, g) January and (b, d, f, h) February. Vectors in (e, f) represent the WAF (unit: m^2 s^{-2}) associated with Z200 anomalies in (e) January and (f) February. Dark-gray and light-gray shadings in (a, b) represent the significance level at 90% and 80% confidence levels, respectively. Stippling in (c–h) and red contour lines in (e, f) denote the 90% confidence level using Student's *t*-test.

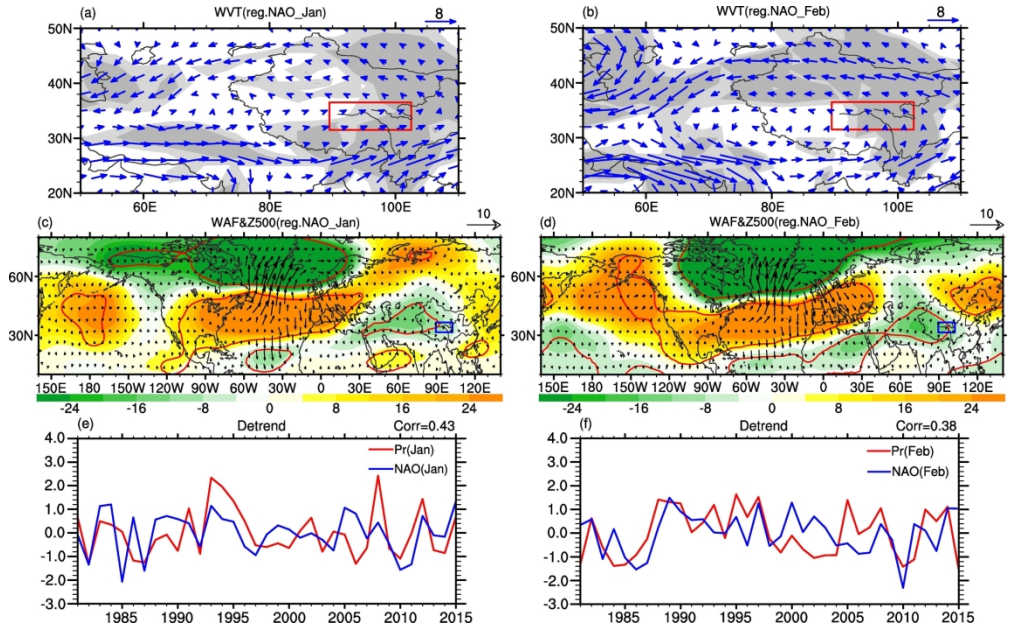

FIGURE 7 Anomalies of (a, b) vertically integrated WVT (unit: kg m^{-1} s^{-1}), (c, d) Z500 (colored shading, unit: gpm) regressed on the detrended and standardized NAO index in (a, c) January and (b, d) February, (e, f) shows detrended and standardized time series of TRS precipitation (Pr; red) and NAO index (blue) in (e) January and (f) February, with the correlation coefficient labeled in the top-right corner. Vectors in (c, d) represent the WAF (unit: m^2 s^{-2}) associated with Z500 anomalies in (c) January and (d) February. Gray shadings in (a, b) and stippling in (c, d) denote the 90% confidence level using Student's *t*-test.

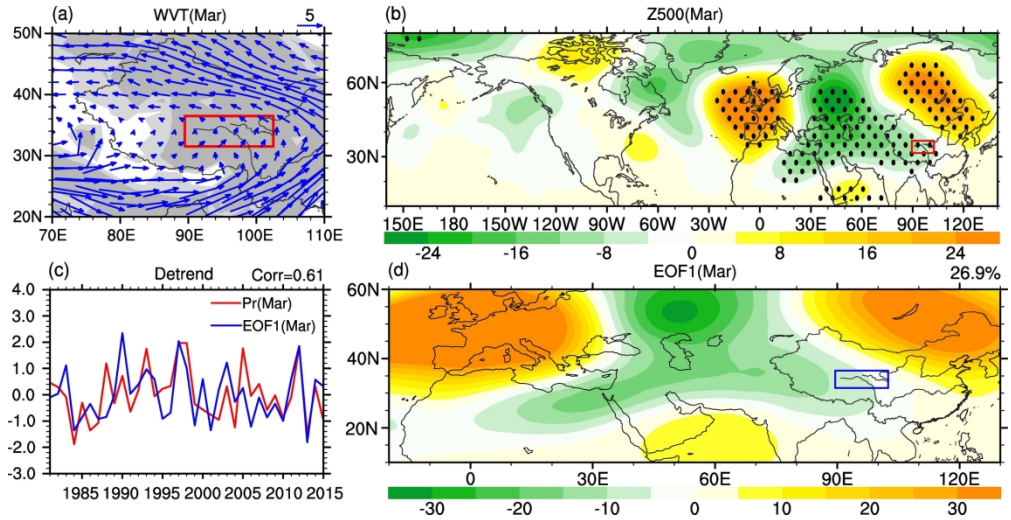

FIGURE 8 Anomalies of (a) vertically integrated WVT (unit: kg m^{-1} s^{-1}), (b) Z500 (unit: gpm) regressed on the detrended and standardized time series of TRS precipitation in March, (c) shows the detrended and standardized time series of TRS precipitation (Pr; red) and time series of the leading EOF mode of Z500 over Eurasia (EOF1; 10°–60°N, 20°W–130°E; blue) in March, with the correlation coefficient labeled in the top-right corner, (d) Leading EOF mode of Z500 over Eurasia (10°–60°N, 20°W–130°E) in March, with the explained variance labeled in the top-right corner. Dark-gray and light-gray shadings in (a) represent the significance level at 90% and 80% confidence levels, respectively. Stippling in (b) denotes the 90% confidence level using Student's *t*-test.

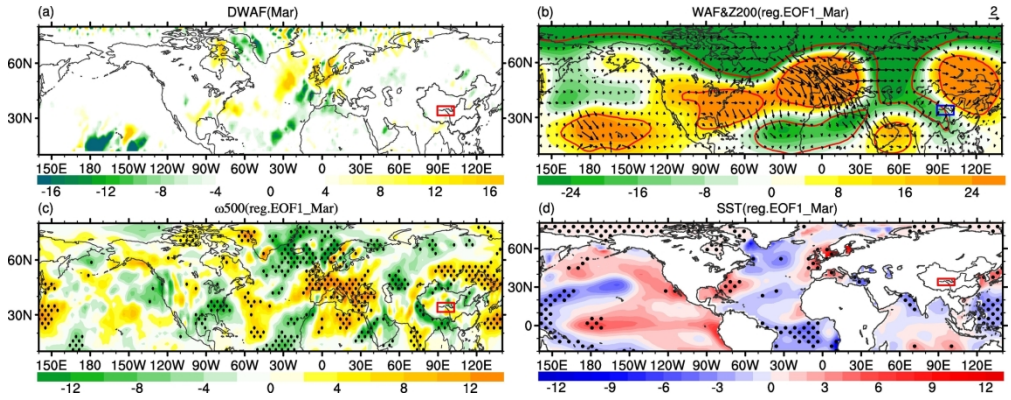

FIGURE 9 (a) Divergence of wave activity flux (DWAF, unit: 10^5 m s^{-2}), anomalies of (b) Z200 (colored shading, unit: gpm), (c) 500-hPa vertical velocity (ω500, unit: 10^2 Pa s^{-1}, negative values represent upward motion and vice versa), (d) SST (unit: 10 ℃) regressed on the detrended and standardized time series of the leading EOF mode of Z500 over Eurasia (EOF1; 10°–60°N, 20°W–130°E) in March. Vectors in (b) represent the WAF (unit: m^2 s^{-2}) associated with Z200 anomalies. Stippling in (c, d) and red contour lines in (b) denote the 90% confidence level using Student's *t*-test.

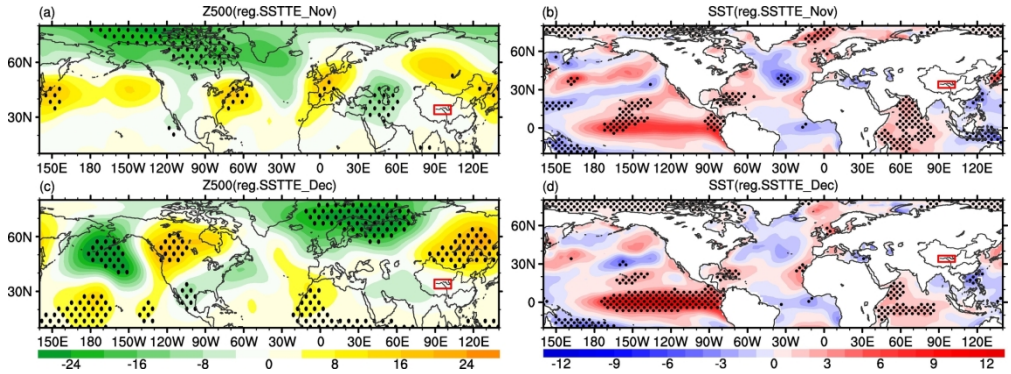

FIGURE 10 Anomalies of (a, c) Z500 (unit: gpm), (b, d) SST (unit: 10 ℃) in (a, b) November and (c, d) December regressed on the detrended and standardized time series of the SST tendency (SSTTE) index (subtract the November Niño 3 index from the December Niño 3 index). Stippling denotes the 90% confidence level using the Student's *t*-test.